HHS Public Access

Author manuscript

Biomaterials. Author manuscript; available in PMC 2020 October 01.

Published in final edited form as:

Biomaterials. 2019 October ; 218: 119365. doi:10.1016/j.biomaterials.2019.119365.

In situ polymerization on nanoscale metal-organic frameworks for enhanced physiological stability and stimulus-responsive intracellular drug delivery

Yuan Liu[a], **Christina S. Gong**[a], **Yunlu Dai**[a], **Zhen Yang**[a], **Guocan Yu**[a], **Yijing Liu**[a], **Mingru Zhang**[a], **Lisen Lin**[a], **Wei Tang**[a], **Zijian Zhou**[a], **Guizhi Zhu**[a], **Jiji Chen**[b], **Orit Jacobson**[a], **Dale O. Kiesewetter**[a], **Zhantong Wang**[a], **Xiaoyuan Chen**[a]

[a]Laboratory of Molecular Imaging and Nanomedicine, National Institute of Biomedical Imaging and Bioengineering, National Institutes of Health, Bethesda, Maryland 20892, United States

[b]Advanced Imaging and Microscopy Resource, National Institute of Biomedical Imaging and Bioengineering, National Institutes of Health, Bethesda, Maryland 20892, United States

Abstract

Metal-organic framework (MOF) nanoparticles have shown great potential as carrier platforms in theranostic applications. However, their poor physiological stability in phosphate-based media has limited their biological applications. Here, we studied the dissociation of MOF nanoparticles under physiological conditions, both *in vitro* and *in vivo*, and developed an *in situ* polymerization strategy on MOF nanoparticles for enhanced stability under physiological conditions and stimulus-responsive intracellular drug release. With polymer wrapped on the surface serving as a shield, the nanoscale MOFs were protected from decomposition by phosphate ions or acid and prevented the loaded cargos from leaking. An *in vivo* positron emission tomography (PET) study of ^{64}Cu-labeled porphyrinic MOF indicated prolonged circulation time of the *in situ* polymerized MOF nanoparticles and greater tumor accumulation than unmodified MOF nanoparticles. With enhanced stability, cargos loaded into MOF nanoparticles or prodrugs conjugated on the surface can be efficiently delivered and released upon stimulus-responsive cleavage.

Keywords

metal-organic framework; polymerization; PET; stimulus-responsive drug delivery

1. Introduction

Metal-organic frameworks (MOFs) have attracted great attention in catalysis [1-6], energy [7-10], and biomedical [11-16] applications owing to their unique physicochemical properties. Their porous structure enables MOF to be an ideal candidate for cargo storage

Corresponding authors: zhantong.wang@nih.gov; shawn.chen@nih.gov.

Date Availability

The raw/processed data required to reproduce these findings cannot be shared at this time as the data also forms part of an ongoing study.

and transport [17, 18]. Various nanoscale MOFs have been prepared for bioimaging [19-23], drug delivery [24-27], and immunotherapy [28]. MOFs typically offer controlled structure, tunable porosity, and chemical functionalization, making them good examples as multifunctional nanocarriers [29-32]. However, the poor physiological stability of MOFs has significantly limited their biochemical applications. For example, zinc-based MOFs typically have poor stability in water, especially in acidic aqueous buffers [33-35]. Zirconium-based MOFs are very sensitive to phosphate-containing buffers, such as phosphate buffered saline (PBS) [36] and RPMI-1640, both of which have relatively high concentrations of phosphate ion. This sensitivity is due to a stronger binding affinity between Zr and the guest phosphate ion [37, 38]. Thus, a high concentration of phosphate ion *in vivo* is fatal for ZrMOF.

So far, tumor therapy with ZrMOF nanoparticles through tail vein injection has rarely been applied due to their poor stability [39, 40]. Metal-free covalent organic frameworks have good stability, but the poor biocompatibility has limited their biochemical applications [41-45]. To facilitate the bioapplications of MOFs, the external surface functionalization of MOF nanoparticles have been realized through coordinative binding on unsaturated metal sites, covalent binding to prefunctionalized linkers, and ligand exchange [46-50]. Despite the success of external surface functionalization [51-54], only very few facile and generalizable stimulus-responsive intracellular drug release systems have been achieved [55-59]. Although phosphate ion can trigger the decomposition of many Zr-based MOFs, phosphate responsive drug delivery using uniform porous MOF nanoparticles as the carrier has not been reported yet, because the decomposition of MOFs by physiological phosphate ion is not controllable, especially in an *in vivo* environment. The *in vivo* concentrations of phosphate ion (1 mM extracellular) and phosphocreatine, which is typically present intracellularly at 20 times the apparent free intracellular phosphate concentration of 0.5–5 mM, are sufficient to decompose ZrMOF quickly upon intravenous injection [60]. So, it is highly desirable to design a ZrMOF nanoparticle with high physiological stability and phosphate stimuli-responsive function to facilitate the biomedical applications of MOF nanoparticles.

2. Experimental section

2.1. Materials

All reagents used were purchased from Sigma-Aldrich, unless otherwise stated. N,N'-bis(acryloyl)cystamine and GSH were purchased from Fisher Scientific. Poly(ethylene glycol) diacrylate and fluorescein dimethacrylate were purchased from Polyscience, Inc. Singlet oxygen sensor green (SOSG) and fetal bovine serum were purchased from Invitrogen. Meso-tetra(4-carboxyphenyl) porphine (TCPP) was purchased from Frontier Scientific. The water used was purified on a Milli-Q Biocell System. All above chemicals were used as received without further processing. The A431 cell line and U87MG human glioblastoma cell line were obtained from the American Type Culture Collection and cultured with RPMI 1640 (RPMI) in a cell culture flask. Athymic nude mice were purchased from Envigo laboratories. The tumor model was established by subcutaneously injection of around 5×10^6 A431 cells into the mice left hind limb. All the experimental procedures had been conducted following a protocol approved by the animal care and use committee (ACUC) of the National Institutes of Health Clinical Center (NIHCC).

2.2. Characterization

Transmission electron microscopy (TEM) images were acquired on a Tecnai TF30 transmission electron microscope (TEM) (FEI, Hillsboro, OR). UV-Vis absorption was measured by a Genesys 10S UV-vis spectrophotometer. NMR: ZrMOF, ZrMOF-PAA, ZrMOF-PAC, and ZrMOF-PEG were dissolved thoroughly by concentrated PBS (10X). A dialysis was conducted to each sample after decomposing. The released polymers were then dried for NMR measurement. The X-ray diffraction measurements were performed on a Bruker D8 ADVANCE diffractometer, employing the standard setup in reflection geometry. The concentrations of platinum were collected by inductively coupled plasma optical emission spectroscopy (ICP-OES, Agilent 720-ES). Microscopy imaging of poly-FITC-wrapped UiO-66 nanoparticles was obtained from an Advanced Imaging and Microscopy Resource at the National Institutes of Health. The imaging experiments were conducted on a custom-built Olympus IX 71 microscope coupled with a 150X oil-immersion objective lens (Olympus, N.A. = 1.45), a multi-band dichroic (405/488/561/633 BrightLine quad-band bandpass filter, Semrock, USA) and a piezo z-stage (Madcity Lab, USA). The laser (488 nm, Spectra-Physics) was focused into the back-pupil plane of the objective to generate wide-field illumination. An xy translation stage with a mirror was placed in the conjugated back pupil plane to steer the laser beam for generating TIRF or HILO illumination. The emission was collected by the same objective passing through a quad-band bandpass filter (FF01-446/523/600/677-25, Semrock, USA) in front of the electron-multiplying charge-coupled device (EMCCD) (iXon DU-888, Andor Technologies). The microscope, AOTF, lasers and the camera were controlled through μ-manager.

2.3. Synthesis of MOF nanoparticles

Synthesis of zirconum-based porphyrinic MOF (ZrMOF) nanoparticles [61]: In a typical synthesis, ZrOCl2 (30 mg), meso-tetra(4-carboxyphenyl)porphyrin (TCPP) (10 mg) and benzoic acid (280 mg) were dissolved in 10 mL of DMF in a 20 mL vial. The solution was sonicated and incubated in an oil bath at 90 °C for 5 h. The resulting product was collected by centrifugation, and washed with DMF and resuspended in DMF for further use.

Synthesis of MIL-101 (Fe) [62]: Typically, iron (III) chloride hexahydrate and 1,4-benzenedicarboxylic acid were dissolved in DMF and then incubated in an oil bath for 15 minutes at 150 °C. After cooling, MIL-101 (Fe) nanoparticles were washed with DMF and redispersed in DMF for future use.

Synthesis of ZIF-8 [34]: In a typical synthesis of 50 nm ZIF-8 nanoparticles, Zn(NO3)2 (150 mg) was dissolved in 7 mL of methanol. Then, 2-methylimidazole (330 mg) was dissolved in 7 mL of methanol, and injected into the Zn solution with vigorous stirring. After 5 minutes, the mixture turned cloudy. The reaction was stopped and the ZIF-8 nanoparticles were washed with methanol and resuspended in DMF for further use.

Synthesis of UiO-66 nanoparticles [63]: To synthesize UiO-66 nanoparticles, 1,4-benzenedicarboxylic acid (100 mg) was dissolved in 1 mL of DMF, and zirconyl chloride octahydrate (21 mg) was dissolved in 3 mL of DMF. The two solutions were then mixed together, followed by adding 2 mL of glacial acetic acid. The resulting solution was

incubated in an oil bath for 12 h at 120 °C. UiO-66 nanoparticles were washed with DMF before further use.

2.4. *In situ* polymerization on MOF nanoparticles

The ligand bis[2-(methacryloyloxy)ethyl] phosphate (BMAP) was first anchored on the surface of MOF nanoparticles. Typically, BMAP (2.5 mM, 300 μL) was added to MOF nanoparticles (ZrMOF, MIL-101 (Fe), UiO-66, and ZIF-8) in DMF and incubated for 5 h at room temperature. Free BMAP was removed by washing with DMF and the MOF NPs were redispersed in DMF. Then, azobisisobutyronitrile (AIBN) and monomers (such as N, N'-bis(acryloyl) cystamine, acrylic acid, poly(ethylene glycol) diacrylate, fluorescein dimethacrylate, and poly(ethylene glycol) methyacrylate) were added to the BMAP-modified MOF nanoparticle solution and incubated for 10 h at 65 °C. The polymer-wrapped MOF nanoparticles were then washed with DMF and water and finally redispersed in PBS buffer for further study.

2.5. Stability study

MOF nanoparticles (ZrMOF, MIL-101 (Fe), ZIF-8) and polymer-wrapped MOF nanoparticles were dispersed in PBS, RPMI-1640, or sodium acetate buffer. In the time-dependent study, MOF nanoparticles were characterized by TEM and UV-vis at different periods of time. In the concentration-dependent study, MOF nanoparticles were dispersed in different concentrations of PBS buffer and finally characterized by TEM.

2.6. Cisplatin loading

To load the cisplatin into the ZrMOF nanoparticles, 0.5 mL (10 mg/mL) of cisplatin in DMF was added to the ZrMOF nanoparticles solution and incubated overnight at 50 °C on a shaking table. Cisplatin-loaded ZrMOF nanoparticles were then washed with DMF and redispersed in DMF for further polymerization.

2.7. Synthesis of ligands

Synthesis of methacrylate-disulfide-camptothecin (CPT) [64]: Part 1. Synthesis of 2-((2-hydroxyethyl)disulfanyl)ethyl methacrylate. Dry tetrahydrofuran (THF) (100 mL), 2,2'-dithiodiethanol (20 mmol), and triethylamine (60 mmol) were mixed in a 250 mL round-bottom flask in an ice bath. Methacryloyl chloride (20 mmol) in dry THF (100 mL) was added to the above solution dropwise with vigorous stirring and allowed to react for 12 h at room temperature. After evaporating the solvent, the residue was dissolved in ethyl acetate and then washed twice with water and brine. The organic layer was dried over anhydrous $MgSO_4$ and concentrated. Finally, silica gel column chromatography was used to purify the product using ethyl acetate/petroleum ether (1/3) as the eluent. Part 2. Synthesis of methacrylate-disulfide-CPT. Two gram of CPT and 2.11 g of DMAP were dispersed in 50 mL of dry dichloromethane under an argon atmosphere. Triphosgene (0.567 g) was added to the above solution and stirred for 30 minutes at room temperature. Dry THF with 1.4 g of 2-((2-hydroxyethyl)disulfanyl)ethyl methacrylate was added dropwise and reacted for 12 h with stirring. The solvent was evaporated and ethyl acetate was added to the residue, which was washed with water, 0.1 M HCl, and, finally, brine. The organic layer was collected and

dried with anhydrous $MgSO_4$. Finally, the crude product was purified by column chromatography using ethyl acetate as the eluent (Fig. S9).

Synthesis of methacrylamide butyl carbozate hydrazine [65]: Tert-butyl carbazate (30 mmol) and triethylamine (36 mmol) were mixed in anhydrous dichloromethane (75 mL) in an ice-water bath. Methacryloyl chloride (30 mmol) in dichloromethane (30 mL) was added to the above solution dropwise and reacted overnight at room temperature. The resulting solution was filtered, and the crude product was purified with silica column chromatography. 1H NMR ($CDCl_3$): 8.25, 6.91 (s, 2H, -NH), 5.40, 6.02(s, 2H, CH_2=), 1.91 (q, 3H, - CH_3), 1.42-1.51 (q, 9H, -$(CH_3)_3$).

2.8. Predrug conjugation

CPT-wrapped MOF nanoparticles: The surface of UiO-66 nanoparticles was first anchored with BMAP through chelation of the Zr ion and phosphate ion. To improve the solubility of CPT-wrapped UiO-66 nanoparticles in aqueous solution, acrylic acid and methacrylate-disulfide-CPT were mixed together with AIBN and reacted for 10 h at 65 °C on a shaking table. The CPT-wrapped-UiO-66 nanoparticles were then washed with DMF and water and finally resuspended in PBS buffer for further study.

DOX-conjugated MOF nanoparticles: The surfaces of UiO-66 nanoparticles were first anchored with BMAP through chelation of the Zr ion and phosphate ion. Methacrylamide butyl carbazate hydrazine was deprotected by trifluoroacetic acid in DMF and then added to BMAP-modified UiO-66 nanoparticles with AIBN and methacrylate PEG-500. The resulting solution was reacted for 10 h at 65 °C on a shaking table. The hydrazine modified UiO-66 nanoparticles were washed with DMF and redispersed in DMF. To conjugate the Dox on the surface of UiO-66 nanoparticles, Dox and triethylamine were added to the hydrazine-modified UiO-66 nanoparticle solution and reacted for overnight at room temperature on a shaking table. Dox-conjugated UiO-66 nanoparticles were washed with water and redispersed in PBS for further study.

2.9. *In vivo* PET imaging

To the as-prepared ZrMOF-PEG nanoparticle solution, ^{64}Cu(Ac)2 (0.7 mCi) was added and incubated at 50 °C for 2 h. The labeling efficiency was monitored by TLC. After labeling, ^{64}Cu-ZrMOF was washed with water and resuspended in PBS buffer at a final concentration of 1 μCi / μL. ^{64}Cu-ZrMOF nanoparticles (100 μCi) were intravenously injected into the A431 tumor-bearing mice. Whole-body PET scans at different periods of time were collected from an Inveon Micro PET scanner (Siemens Medical Solutions). The data were analyzed by 3-dimensional regions of interest using (insert software used). Data were reported as %ID/g.

2.10. *In vitro* cytotoxicity study

MTT assay was conducted to investigate the drug delivery and cytotoxicity. Typically, U87MG cells were seeded in a 96-well plate at a concentration of 5,000 cells per well and cultured at 37 °C, 5% CO_2 for 24 h. The cells were washed with fresh medium, MOF nanoparticles were added, and mixture incubated at 37 °C, 5% CO_2 for 48 h. Then 10 μL of

MTT (5 mg/mL in PBS) was added to the cells and incubated for 4 h. Finally, the medium was replaced with 100 μL of DMSO. The absorbance of each well was measured at 490 nm with plate reader.

2.11. Confocal microscopy

The U87MG cells were first seeded in an 8-well Lab-Tek cover-glass slide with a concentration of 25,000 cells per well. Dox conjugated UiO-66 nanoparticles or Poly-FITC-wrapped UiO-66 nanoparticles were added and incubated with cells for 2 hours at 37 °C, 5% CO2. After washing with PBS for three times, Z-Fix solution was added to fix the cells at 37 °C, 5% CO2 for 20 min. Mounting medium with DAPI was then added to stain for 30 min. Confocal images were obtained from a fluorescence microscope (Zeiss LSM 780).

2.12. Stability of ^{64}Cu labeling

The stability of ^{64}Cu-labeled ZrMOF was studied using cell culture medium DMEM with 10% FBS and mouse serum. To monitor the stability of ^{64}Cu-ZrMOF, ITLC was conducted at 1, 24, and 48 h. As shown in Fig. S17 and Fig. S18, the labeling is stable in cell culture medium DMEM and mouse serum, with negligible amount of free ^{64}Cu observed after 48 h.

3. Results and discussion

We opined that coating of MOF nanoparticles with a functionalized polymer would provide inherent physiological stability to the encased MOF and provide a mechanism for stimuli-responsive decomposition of the particle. We developed a novel *in situ* polymerization on the surface of MOF nanoparticles. The polymer wrapped surface, as depicted in scheme 1, of nanoscale MOF protects the particles from decomposition by acid or phosphate ions is expected to increase their circulation time and allow the particles to successfully transport their cargo to the target. We studied several monomers for the *in situ* polymerization including methacrylic acid, poly(ethylene glycol) methyl ether acrylate, fluorescein dimethylacrylate and bis(acryloyl) cystamine. Bis(acryloyl) cystamine provides a crosslinked polymer whose decomposition can be stimulated by glutathione in a concentration dependent manner, resulting in exposure of the particle to phosphate and release of encapsulated cargo.

To investigate the stability of polymer-wrapped MOF nanoparticles, various nanoscale MOFs were synthesized, including PCN-224 (ZrMOF), MIL-101 (Fe), ZIF-8, and UiO-66. These MOF nanoparticles were characterized by TEM and XRD, as shown in Fig. 1 and Fig. S12-S15. In a typical preparation of polymer-wrapped MOF nanoparticles, the surfaces of the as-prepared MOF nanoparticles were first anchored with bis[2-(methacryloyloxy)ethyl] phosphate (BMAP), due to the strong binding affinity between Zr and phosphate, as shown in scheme 1. Because excess amount of BMAP can decompose MOF nanoparticles, an optimization experiment was conducted to determine the concentration of BMAP. Thereafter, 2.5 mM (300 μL) of BMAP was used for ligand anchoring to 500 μL of MOF nanoparticles (1 mg/mL).

To wrap functional polymer on the surfaces of MOF nanoparticles, different monomers, bis(acryloyl)cystamine, poly(ethylene glycol) diacrylate, fluorescein dimethacrylate, and

acrylic acid were incubated, respectively, with different BMAP-MOF nanoparticles. The radical initiator, AIBN, was introduced to start the polymerization onto the BMAP, which built up the surface coating. Upon obtaining poly(N,N'-bis(acryloyl)cystamine)-wrapped ZrMOF (ZrMOF-PAC), poly(acrylic acid)-wrapped MIL-101 (MIL-PAA), and poly(ethylene glycol)-wrapped ZIF-8 (ZIF-PEG) nanoparticles, the NPs were treated with different buffers to test their respective stabilities. As shown in Fig. 1, without polymer coating ZrMOF and MIL-101 (Fe) were decomposed quickly in PBS buffer, while ZrMOF-PAC and MIL-PAA were still very stable in PBS even after 15 h. ZIF-8 nanoparticles were decomposed immediately and completely upon adding sodium acetate/acetic acid buffer (pH=5.5) (Fig. S1), while ZIF-PEG NPs were still stable after 3 h (Fig. 1). These results show that the polymer shield on the surface did, in fact, protect the MOF nanoparticles from decomposing directly by phosphate ions or acidic conditions.

With this *in situ* polymerization approach, ZrMOF-PAA, ZrMOF-PAC, and ZrMOF-PEG nanoparticles were prepared for zeta-potential and dynamic light scattering (DLS) study. As shown in Fig. S2, ZrMOF nanoparticles exhibited slightly positive surface charge. ZrMOF-PAC and ZrMOF-PEG nanoparticles showed neutral surface charge, while ZrMOF-PAA nanoparticles exhibited negative surface charge. DLS indicated that ZrMOF showed a good colloidal stability before and after polymerization. A slight increment in size was observed after *in situ* polymerization (Fig. S16). The infrared spectra of ZrMOF and polymer-wrapped ZrMOF nanoparticles were analyzed (Fig. 3A). The characteristic amide group peak (around 3300 cm-1) and the C-H stretch peak from bis(acrylol) cystamine were observed in the spectrum of ZrMOF-PAC. In addition, the characteristic peaks of acrylic acid and ethylene glycol (CH2 around 2900 cm-1) were also observed after polymerization on the surface of ZrMOF nanoparticles. Similiar characteristic peaks were observed in the case of UiO-66 and polymer-wrapped UiO-66 nanoparticles as well, as shown in Fig. 3B. To characterize the polymer on the surface of ZrMOF with NMR, ZrMOF nanoparticles were decomposed by concentrated PBS first. The polymers released from ZrMOF were then collected and dried for NMR after dialysis. As shown in Fig. 3C, PAA, PAC, and PEG were confirmed by their characteristic peaks in 1H NMR spectra after releasing from the MOF nanoparticles. We selected ZrMOF-PEG as an example to estimate the associated PEG amount. As shown in Fig. S21, the PEG coating accounts for 14% of ZrMOF-PEG nanoparticles. Furthermore, FITC-wrapped UiO-66 nanoparticles were analyzed by fluorescence spectrometer (Fig. S3) and a custom-built Olympus IX 71 microscope and the image of fluorescent UiO-66 nanoparticles was obtained (Fig. S4). Confocal imaging in Fig. S5 also confirmed that a fluorescent FITC-wrapped UiO-66 nanoparticle exhibited good cellular uptake.

Time-dependent stability studies of ZrMOF, ZrMOF-PAA, and ZrMOF-PAC in 1X PBS were then conducted. As shown in Fig. 2, after 24 h, 29.1%, 25.5%, and 21.1% of TCPP dissociated from ZrMOF, ZrMOF-PAA, and ZrMOF-PAC, respectively, according to the UV-vis absorbance of TCPP in the supernatant. However, 17.8% of TCPP dissociated from ZrMOF, while 4.5% of TCPP dissociated from ZrMOF-PAA, and negligible TCPP dissociated from ZrMOF-PAC after suspending in 1X PBS for 1 h. To monitor the effect of PBS on the crystal structure, ZrMOF and ZrMOF-PAC were selected to conduct a time-dependent XRD comparison. From the XRD-based stability results (Fig. 3D and 3E) , we can see that ZrMOF-PAC is more stable than ZrMOF in PBS. Although both ZrMOF and

ZrMOF-PAC went to amorphous totally after 24 hours, ZrMOF turned to amorphous in 1 hour while ZrMOF-PAC only turned to semi-amorphous in 1 hour. The enhanced stability of ZrMOF-PAC is attributed to the cross-linked polymer PAC which serves as a shield to protect ZrMOF. Time-dependent stability study of ZrMOF-PAA (and ZrMOF PAC) by TEM confirmed confirmed thate collapsing collapse of ZrMOF with time (Fig. S6 and S7). The comparison of Fig. S6 and S7 showed that ZrMOF-PAA is less stable than ZrMOF-PAC at under the same condition. A concentration-dependent stability study of ZrMOF-PAA by TEM indicated that ZrMOF-PAA nanoparticle is very sensitive to high concentration of phosphate ion (Fig. S8).

The stability of ZrMOF in cell culture media is also significant and must be considered when cell viability studies are conducted. Thus, we further tested the stability of nude ZrMOF, ZrMOF-PAA, and ZrMOF-PAC in RPMI-1640, a very commonly used cell culture medium. As seen in Fig. 4, in RPMI medium, nude ZrMOF decomposed quickly in 5 h and ZrMOF-PAA decomposed slowly, while ZrMOF-PAC was most stable among these three types of polymer-wrapped ZrMOFs . The higher stability of ZrMOF-PAC compared to ZrMOF-PAA in PBS may be attributed to the possibility of cross-linked polymerization on ZrMOF-PAC nanoparticles, due to the existence of two polymerization sites on bis(acryloyl)cystamine, while primarily linear polymerization occurs on PAA-ZrMOF nanoparticles.

Having demonstrated an enhanced physiological stability in different media, we then studied the *in vivo* circulation of the polymer-wrapped ZrMOF nanoparticles and their tumor accumulation with PET imaging. The coordination of porphyrin and metal allows the porphyrinic MOF nanoparticle to be labelled with ^{64}Cu, a positron-emitter (Fig. 5A). As shown in theby instant thin layer chromatography (iTLC) graphs (Fig. 5B), ^{64}Cu was stabilized in ZrMOF nanoparticles after two hours incubation at 50 °C. ^{64}Cu-labeled ZrMOF-PEG nanoparticles and ZrMOFs without polymer protection were intravenously injected into A431 tumor-bearing mice. PET images of the mice were collected from a micro-PET scanner at 1, 4, 24, and 48 h after intravenous injection. From Fig. 5C (bottom), ZrMOF without polymerization showed very rapid clearance from the blood. The ZrMOF nanoparticles were collapsed quickly by phosphate ions after injection and formed serious aggregates , which lodged mostly in the lungs and liver. Negligible accumulation in the tumor was observed. However, ZrMOF-PEG nanoparticles showed significant accumulation in the tumor region due to the enhanced permeability and retention effect, as shown in Fig. 5D (top), reaching 4.02 ± 0.38, 4.41 ± 0.24, 5.58 ± 0.41, and 5.09 ± 0.31 %ID/g after 1, 4, 24, and 48 h (Fig. 5d). Further *ex vivo* biodistribution study based on γ-counting of excised organs confirmed this efficient tumor accumulation (Fig. 5E), indicating that a prolonged circulation time was achieved from the *in situ* polymerized ZrMOF-PEG nanoparticles.

Polymerization on the surface of MOF nanoparticles not only increases their stability in buffers and media but it also offers functions such as stimulus-responsive drug delivery. Cisplatin, a chemotherapy drug, can be loaded into the porous ZrMOF and then wrapped with cross-linked PAC polymer. To test this hypothesis, cisplatin-loaded ZrMOF-PAC was used to conduct an intracellular drug delivery study. As illustrated by Fig. 6A and 6B, upon adding GSH, a trigger that initiates the decomposition of PAC, 50% of cisplatin was released

from ZrMOF-PAC nanoparticles according to the ICP analysis. An additional 20% of cisplatin was released gradually due to phosphate ion etching and decomposition of ZrMOF nanoparticles. Without GSH, cisplatin was released gradually with time, and almost 30% of cisplatin was trapped inside the ZrMOF-PAC nanoparticles compared to ZrMOF-PAC with GSH trigger (Fig. 6B). An MTT assay study was further conducted with cisplatin-loaded ZrMOF and cisplatin-loaded ZrMOF-PAC. Without PAC wrapping, the loaded cisplatin leaked seriously when washed with buffer, and relatively poor cancer therapy effect was achieved. Polymer-wrapped ZrMOF-PAC protected the cisplatin from leaking from the ZrMOF nanoparticles and guaranteed effective drug delivery. After cellular uptake, the high level of GSH inside the cancer cells decomposed the cross-linked PAC polymer on the surface of ZrMOF. Upon opening the “doors“, the drug cisplatin was released from the MOF. Phosphate ions inside the cells then etched ZrMOF and accelerated the drug release, thus showing a much better cancer cell therapy effect, as shown in Fig. 6C .

Furthermore, we explored the generalization of this stimuli-responsive drug delivery system using *in situ* polymerization on MOF nanoparticles. A monomer with a CPT as the prodrug and a disulfide bond (Fig. S9) as the stimulus-responsive group was directly polymerized on the surfaces of UiO-66 nanoparticles. To improve the solubility in aqueous solution, polyethylene glycol was mixed with the monomer and co-polymerized (Fig. S10) on the surface of UiO-66 nanoparticles (Fig. 7A). With intracellular GSH stimulus, prodrug CPT was cleaved from the UiO-66 nanoparticles and then killed the cancer cells (Fig. 7C). Another monomer, hydrazine , with polyethylene glycol was also co-polymerized (Fig. S11) on the surface of UiO-66 nanoparticles using the *in situ* polymerization strategy (Fig. 7B). With functional group poly-hydrazine on the surface of UiO-66, Dox was then conjugated on the surface of UiO-66 *via* Wolff-Kishner reduction. Based on the standard curve of Dox (Fig. S19), the conjugated Dox amount was calculated to be 25.1 μmol per gram of ZrMOF. Upon intracellular uptake of Dox-conjugated UiO-66 nanoparticles, the acidic environment in cancer cells initiated a hydrazone hydrolysis and cleaved the Dox from UiO-66 nanoparticles, and the Dox subsequently killed the cancer cells, as shown in Fig. 7C. Both prodrug CPT and Dox-wrapped MOF nanoparticles showed good cancer cell killing efficiency. Furthermore, confocal imaging study confirmed the Dox delivery to cancer cells (Fig. 7D and Fig. S20). Therefore, the *in situ* polymerized prodrug on the surfaces of MOF nanoparticles can not only increase their physiological stability but also enable stimulus-responsive drug release.

4. Conclusion

In conclusion, we studied the stability of different nanoscale MOFs under physiological conditions, both *in vitro* and *in vivo*, and developed an *in situ* polymerization strategy on MOF nanoparticles for enhanced physiological stability, especially in phosphate-based media. A prolonged *in vivo* circulation and greater tumor accumulation with polymer-wrapped ZrMOF nanoparticles was achieved, as shown by PET imaging. With enhanced stability, stimulus-responsive drug delivery was then achieved using porous ZrMOF nanoparticles. Moreover, the *in situ* polymerization enables the prodrug to both increase the stability of MOF nanoparticles and responsively release the drug intracellularly. The polymer-wrapped MOF nanoparticles provide a robust, efficient and safe drug delivery

platform for theranostics. Based on these superior features, future tumor therapy with intravenous injection should be conducted to encourage further clinical study.

Supplementary Material

Refer to Web version on PubMed Central for supplementary material.

Acknowledgements

The authors are grateful to Dr. YuHuang Wang for his help on thermogravimetric analysis. This work supported by the Intramural Research Program of the National Institute of Biomedical Imaging and Bioengineering (NIBIB), National Institutes of Health (NIH).

References

[1]. Feng D, Gu ZY, Li JR, Jiang HL, Wei Z, Zhou HC, Zirconium-metalloporphyrin PCN-222: mesoporous metal–organic frameworks with ultrahigh stability as biomimetic catalysts, Angew. Chem. Int. Ed. 51(41) (2012) 10307–10310.

[2]. Li P, Moon S-Y, Guelta MA, Lin L, Gómez-Gualdrón DA, Snurr RQ, Harvey SP, Hupp JT, Farha OK, Nanosizing a metal–organic framework enzyme carrier for accelerating nerve agent hydrolysis, ACS Nano 10 (2016) 9174–9182. [PubMed: 27701869]

[3]. Li Z, Peters AW, Platero-Prats AE, Liu J, Kung C-W, Noh H, DeStefano MR, Schweitzer NM, Chapman KW, Hupp JT, Fine-Tuning the Activity of Metal–Organic Framework-Supported Cobalt Catalysts for the Oxidative Dehydrogenation of Propane, J. Am. Chem. Soc. 139 (2017) 15251–15258. [PubMed: 28976757]

[4]. Yoon M, Srirambalaji R, Kim K, Homochiral metal–organic frameworks for asymmetric heterogeneous catalysis, Chem. Rev. 112 (2011) 1196–1231. [PubMed: 22084838]

[5]. Zhao M, Yuan K, Wang Y, Li G, Guo J, Gu L, Hu W, Zhao H, Tang Z, Metal–organic frameworks as selectivity regulators for hydrogenation reactions, Nature 539 (2016) 76. [PubMed: 27706142]

[6]. Zhu L, Liu X-Q, Jiang H-L, Sun L-B, Metal–organic frameworks for heterogeneous basic catalysis, Chem. Rev. 117 (2017) 8129–8176. [PubMed: 28541694]

[7]. Eddaoudi M, Kim J, Rosi N, Vodak D, Wachter J, O'keeffe M, Yaghi OM, Systematic design of pore size and functionality in isoreticular MOFs and their application in methane storage, Science 295 (2002) 469–472. [PubMed: 11799235]

[8]. Farha OK, Yazaydın AÖ, Eryazici I, Malliakas CD, Hauser BG, Kanatzidis MG, Nguyen ST, Snurr RQ, Hupp JT, De novo synthesis of a metal–organic framework material featuring ultrahigh surface area and gas storage capacities, Nat. Chem. 2 (2010) 944. [PubMed: 20966950]

[9]. Furukawa H, Cordova K, Keeffe O, Yaghi M, OM, Science 341 (2013) 1230444. [PubMed: 23990564]

[10]. Yuan D, Zhao D, Sun D, Zhou HC, An Isoreticular Series of Metal–Organic Frameworks with Dendritic Hexacarboxylate Ligands and Exceptionally High Gas-Uptake Capacity, Angew. Chem. Int. Ed. 122 (2010) 5485–5489.

[11]. He C, Liu D, Lin W, Nanomedicine applications of hybrid nanomaterials built from metal–ligand coordination bonds: nanoscale metal–organic frameworks and nanoscale coordination polymers, Chem. Rev. 115 (2015) 11079–11108. [PubMed: 26312730]

[12]. Horcajada P, Gref R, Baati T, Allan PK, Maurin G, Couvreur P, Ferey G, Morris RE, Serre C, Metal–organic frameworks in biomedicine, Chem. Rev. 112 (2011) 1232–1268. [PubMed: 22168547]

[13]. Liu D, Huxford RC, Lin W, Phosphorescent nanoscale coordination polymers as contrast agents for optical imaging, Angew. Chem. Int. Ed. 50 (2011) 3696–3700.

[14]. Simon-Yarza T, Mielcarek A, Couvreur P, Serre C, Nanoparticles of Metal-Organic Frameworks: On the Road to In Vivo Efficacy in Biomedicine, Adv. Mater. 30 (2018) 1707365.

[15]. Wang S, McGuirk CM, d'Aquino A, Mason JA, Mirkin CA, Metal–organic framework nanoparticles, Adv. Mater. 30 (2018) 1800202.

[16]. Cai X, Liu B, Pang M, Lin J, Interfacially synthesized Fe-soc-MOF nanoparticles combined with ICG for photothermal/photodynamic therapy, Dalton Trans. 47 (2018) 16329–16336. [PubMed: 30403239]

[17]. Horcajada P, Chalati T, Serre C, Gillet B, Sebrie C, Baati T, Eubank JF, Heurtaux D, Clayette P, Kreuz C, Porous metal–organic-framework nanoscale carriers as a potential platform for drug delivery and imaging, Nat. Mater. 9 (2010) 172. [PubMed: 20010827]

[18]. Zheng H, Zhang Y, Liu L, Wan W, Guo P, Nyström AM, Zou X, One-pot synthesis of metal–organic frameworks with encapsulated target molecules and their applications for controlled drug delivery, J. Am. Chem. Soc. 138 (2016) 962–968. [PubMed: 26710234]

[19]. Huang X, He Z, Guo D, Liu Y, Song J, Yung BC, Lin L, Yu G, Zhu J-J, Xiong Y, "Three-in-one" Nanohybrids as Synergistic Nanoquenchers to Enhance No-Wash Fluorescence Biosensors for Ratiometric Detection of Cancer Biomarkers, Theranostics 8 (2018) 3461. [PubMed: 30026859]

[20]. Liu Y, Hou W, Xia L, Cui C, Wan S, Jiang Y, Yang Y, Wu Q, Qiu L, Tan W, ZrMOF nanoparticles as quenchers to conjugate DNA aptamers for target-induced bioimaging and photodynamic therapy, Chem. Sci. 9 (2018) 7505–7509. [PubMed: 30319750]

[21]. Morris W, Briley WE, Auyeung E, Cabezas MD, Mirkin CA, Nucleic acid–metal organic framework (MOF) nanoparticle conjugates, J. Am. Chem. Soc. 136 (2014) 7261–7264. [PubMed: 24818877]

[22]. Wang S, McGuirk CM, Ross MB, Wang S, Chen P, Xing H, Liu Y, Mirkin CA, General and direct method for preparing oligonucleotide-functionalized metal–organic framework Nanoparticles, J. Am. Chem. Soc. 139 (2017) 9827–9830. [PubMed: 28718644]

[23]. Wang XG, Cheng Q, Yu Y, Zhang XZ, Controlled Nucleation and Controlled Growth for Size Predicable Synthesis of Nanoscale Metal–Organic Frameworks (MOFs): A General and Scalable Approach, Angew. Chem. Int. Ed. 57 (2018) 7836–7840.

[24]. Chen W, Wu C, Synthesis, functionalization, and applications of metal–organic frameworks in biomedicine, Dalton Trans. 47 (2018) 2114–2133. [PubMed: 29369314]

[25]. He C, Lu K, Liu D, Lin W, Nanoscale metal–organic frameworks for the co-delivery of cisplatin and pooled siRNAs to enhance therapeutic efficacy in drug-resistant ovarian cancer cells, J. Am. Chem. Soc. 136 (2014) 5181–5184. [PubMed: 24669930]

[26]. Lan G, Ni K, Xu Z, Veroneau SS, Song Y, Lin W, Nanoscale metal–organic framework overcomes hypoxia for photodynamic therapy primed cancer immunotherapy, J. Am. Chem. Soc. 140 (2018) 5670–5673. [PubMed: 29665677]

[27]. Wuttke S, Lismont M, Escudero A, Rungtaweevoranit B, Parak WJ, Positioning metal-organic framework nanoparticles within the context of drug delivery–a comparison with mesoporous silica nanoparticles and dendrimers, Biomaterials 123 (2017) 172–183. [PubMed: 28182958]

[28]. Lu K, He C, Guo N, Chan C, Ni K, Lan G, Tang H, Pelizzari C, Fu Y-X, Spiotto MT, Low-dose X-ray radiotherapy–radiodynamic therapy *via* nanoscale metal–organic frameworks enhances checkpoint blockade immunotherapy, Nat. Biomed. Eng. 2 (2018) 600. [PubMed: 31015630]

[29]. Freund R, Lächelt U, Gruber T, Rühle B, Wuttke S, Multifunctional efficiency: Extending the concept of atom economy to functional nanomaterials, ACS Nano 12 (2018) 2094–2105. [PubMed: 29533060]

[30]. Lan G, Ni K, Xu R, Lu K, Lin Z, Chan C, Lin W, Nanoscale metal–organic layers for deeply penetrating X-ray-induced photodynamic therapy, Angew. Chem. Int. Ed. 129 (2017) 12270–12274.

[31]. Lismont M, Dreesen L, Wuttke S, Metal-Organic Framework Nanoparticles in Photodynamic Therapy: Current Status and Perspectives, Adv. Func. Mater. 27 (2017) 1606314.

[32]. Ma Y, Li X, Li A, Yang P, Zhang C, Tang B, H2S-activable MOF nanoparticle photosensitizer for effective photodynamic therapy against cancer with controllable singlet-oxygen release, Angew. Chem. Int. Ed. 56 (2017) 13752–13756.

[33]. Duan Y, Ye F, Huang Y, Qin Y, He C, Zhao S, One-pot synthesis of a metal–organic framework-based drug carrier for intelligent glucose-responsive insulin delivery, Chem. Commun. 54 (2018) 5377–5380.

[34]. Zhuang J, Kuo C-H, Chou L-Y, Liu D-Y, Weerapana E, Tsung C-K, Optimized metal–organic-framework nanospheres for drug delivery: evaluation of small-molecule encapsulation, ACS Nano 8 (2014) 2812–2819. [PubMed: 24506773]

[35]. Yue Y, Qiao Z-A, Li X, Binder AJ, Formo E, Pan Z, Tian C, Bi Z, Dai S, Nanostructured zeolitic imidazolate frameworks derived from nanosized zinc oxide precursors, Crystal Growth & Design 13 (2013) 1002–1005.

[36]. Chen Y, Li P, Modica JA, Drout RJ, Farha OK, Acid-Resistant Mesoporous Metal–Organic Framework toward Oral Insulin Delivery: Protein Encapsulation, Protection, and Release, J. Am. Chem. Soc. 140 (2018) 5678–5681. [PubMed: 29641892]

[37]. Deria P, Bury W, Hod I, Kung C-W, Karagiaridi O, Hupp JT, Farha OK, MOF functionalization *via* solvent-assisted ligand incorporation: Phosphonates vs carboxylates, Inorg. Chem. 54 (2015) 2185–2192. [PubMed: 25665089]

[38]. Wang S, Morris W, Liu Y, McGuirk CM, Zhou Y, Hupp JT, Farha OK, Mirkin CA, Surface-Specific Functionalization of Nanoscale Metal–Organic Frameworks, Angew. Chem. Int. Ed. 54 (2015) 14738–14742.

[39]. Lu K, He C, Lin W, Nanoscale metal–organic framework for highly effective photodynamic therapy of resistant head and neck cancer, J. Am. Chem. Soc. 136 (2014) 16712–16715. [PubMed: 25407895]

[40]. Ni K, Lan G, Chan C, Quigley B, Lu K, Aung T, Guo N, La Riviere P, Weichselbaum RR, Lin W, Nanoscale metal-organic frameworks enhance radiotherapy to potentiate checkpoint blockade immunotherapy, Nat. Commun. 9 (2018) 2351. [PubMed: 29907739]

[41]. Diercks CS, Yaghi OM, The atom, the molecule, and the covalent organic framework, Science 355 (2017) eaal1585. [PubMed: 28254887]

[42]. Evans AM, Parent LR, Flanders NC, Bisbey RP, Vitaku E, Kirschner MS, Schaller RD, Chen LX, Gianneschi NC, Dichtel WR, Seeded growth of single-crystal two-dimensional covalent organic frameworks, Science 361 (2018) 52–57. [PubMed: 29930093]

[43]. Ma T, Kapustin EA, Yin SX, Liang L, Zhou Z, Niu J, Li L-H, Wang Y, Su J, Li J, Single-crystal x-ray diffraction structures of covalent organic frameworks, Science 361 (2018) 48–52. [PubMed: 29976818]

[44]. Smith BJ, Parent LR, Overholts AC, Beaucage PA, Bisbey RP, Chavez AD, Hwang N, Park C, Evans AM, Gianneschi NC, Colloidal covalent organic frameworks, ACS Cent. Sci. 3 (2017) 58–65. [PubMed: 28149954]

[45]. Waller PJ, Gándara F, Yaghi OM, Chemistry of covalent organic frameworks, Acc. Chem. Res. 48 (2015) 3053–3063. [PubMed: 26580002]

[46]. Kondo M, Furukawa S, Hirai K, Kitagawa S, Coordinatively immobilized monolayers on porous coordination polymer crystals, Angew. Chem. Int. Ed. 49 (2010) 5327–5330.

[47]. Liu B, Ma M, Zacher D, Bétard A, Yusenko K, Metzler-Nolte N, Wöll C, Fischer RA, Chemistry of SURMOFs: Layer-selective installation of functional groups and post-synthetic covalent modification probed by fluorescence microscopy, J. Am. Chem. Soc. 133 (2011) 1734–1737. [PubMed: 21247137]

[48]. Röder R, Preiß T, Hirschle P, Steinborn B, Zimpel A, Höhn M, Rädler JO, Bein T, Wagner E, Wuttke S, Multifunctional nanoparticles by coordinative self-assembly of His-tagged units with metal–organic frameworks, J. Am. Chem. Soc. 139 (2017) 2359–2368. [PubMed: 28075125]

[49]. Zhu W, Xiang G, Shang J, Guo J, Motevalli B, Durfee P, Agola JO, Coker EN, Brinker CJ, Versatile Surface Functionalization of Metal–Organic Frameworks through Direct Metal Coordination with a Phenolic Lipid Enables Diverse Applications, Adv. Func. Mater. 28 (2018) 1705274.

[50]. Zimpel A, Preiß T, Röder R, Engelke H, Ingrisch M, Peller M, Rädler JO, Wagner E, Bein T, Lächelt U, Imparting functionality to MOF nanoparticles by external surface selective covalent attachment of polymers, Chem. Mater. 28 (2016) 3318–3326.

[51]. Illes B, Hirschle P, Barnert S, Cauda V, Wuttke S, Engelke H, Exosome-coated metal–organic framework nanoparticles: an efficient drug delivery platform, Chem. Mater. 29 (2017) 8042–8046.

[52]. Wang X-G, Dong Z-Y, Cheng H, Wan S-S, Chen W-H, Zou M-Z, Huo J-W, Deng H-X, Zhang X-Z, A multifunctional metal–organic framework based tumor targeting drug delivery system for cancer therapy, Nanoscale 7 (2015) 16061–16070. [PubMed: 26372069]

[53]. Wuttke S, Braig S, Preiß T, Zimpel A, Sicklinger J, Bellomo C, Rädler JO, Vollmar AM, Bein T, MOF nanoparticles coated by lipid bilayers and their uptake by cancer cells, Chem. Commun. 51 (2015) 15752–15755.

[54]. Giménez-Marqués M, Bellido E, Berthelot T, Simón-Yarza T, Hidalgo T, Simón-Vázquez R, González-Fernández Á, Avila J, Asensio MC, Gref R, GraftFast Surface Engineering to Improve MOF Nanoparticles Furtiveness, Small 14 (2018) 1801900.

[55]. Chen W-H, Yu X, Cecconello A, Sohn YS, Nechushtai R, Willner I, Stimuli-responsive nucleic acid-functionalized metal–organic framework nanoparticles using pH-and metal-ion-dependent DNAzymes as locks, Chem. Sci. 8 (2017) 5769–5780. [PubMed: 28989617]

[56]. Dong Z, Sun Y, Chu J, Zhang X, Deng H, Multivariate metal–organic frameworks for dialing-in the binding and programming the release of drug molecules, J. Am. Chem. Soc. 139 (2017) 14209–14216. [PubMed: 28898070]

[57]. Horcajada P, Serre C, Maurin G, Ramsahye NA, Balas F, Vallet-Regi M, Sebban M, Taulelle F, Férey G, Flexible porous metal-organic frameworks for a controlled drug delivery, J. Am. Chem. Soc. 130 (2008) 6774–6780. [PubMed: 18454528]

[58]. Tan L-L, Li H, Qiu Y-C, Chen D-X, Wang X, Pan R-Y, Wang Y, Zhang SX-A, Wang B, Yang Y-W, Stimuli-responsive metal–organic frameworks gated by pillar [5] arene supramolecular switches, Chem. Sci. 6 (2015) 1640–1644. [PubMed: 30154997]

[59]. Wu MX, Yang YW, Metal–organic framework (MOF)-based drug/cargo delivery and cancer therapy, Adv. Mater. 29 (2017) 1606134.

[60]. Bergwitz C, Jüppner H, Phosphate sensing, Adv. Chronic Kidney Dis. 18 (2011) 132–144. [PubMed: 21406298]

[61]. Park J, Jiang Q, Feng D, Mao L, Zhou H-C, Size-controlled synthesis of porphyrinic metal–organic framework and functionalization for targeted photodynamic therapy, J. Am. Chem. Soc. 138 (2016) 3518–3525. [PubMed: 26894555]

[62]. Taylor-Pashow KM, Della Rocca J, Xie Z, Tran S, Lin W, Postsynthetic modifications of iron-carboxylate nanoscale metal− organic frameworks for imaging and drug delivery, J. Am. Chem. Soc. 131 (2009) 14261–14263. [PubMed: 19807179]

[63]. Katz MJ, Brown ZJ, Colón YJ, Siu PW, Scheidt KA, Snurr RQ, Hupp JT, Farha OK, A facile synthesis of UiO-66, UiO-67 and their derivatives, Chem. Commun. 49 (2013) 9449–9451.

[64]. Hu X, Hu J, Tian J, Ge Z, Zhang G, Luo K, Liu S, Polyprodrug amphiphiles: hierarchical assemblies for shape-regulated cellular internalization, trafficking, and drug delivery, J. Am. Chem. Soc. 135 (2013) 17617–17629. [PubMed: 24160840]

[65]. Xu Z, Zhang K, Hou C, Wang D, Liu X, Guan X, Zhang X, Zhang H, A novel nanoassembled doxorubicin prodrug with a high drug loading for anticancer drug delivery, J. Mater. Chem. B 2 (2014) 3433–3437.

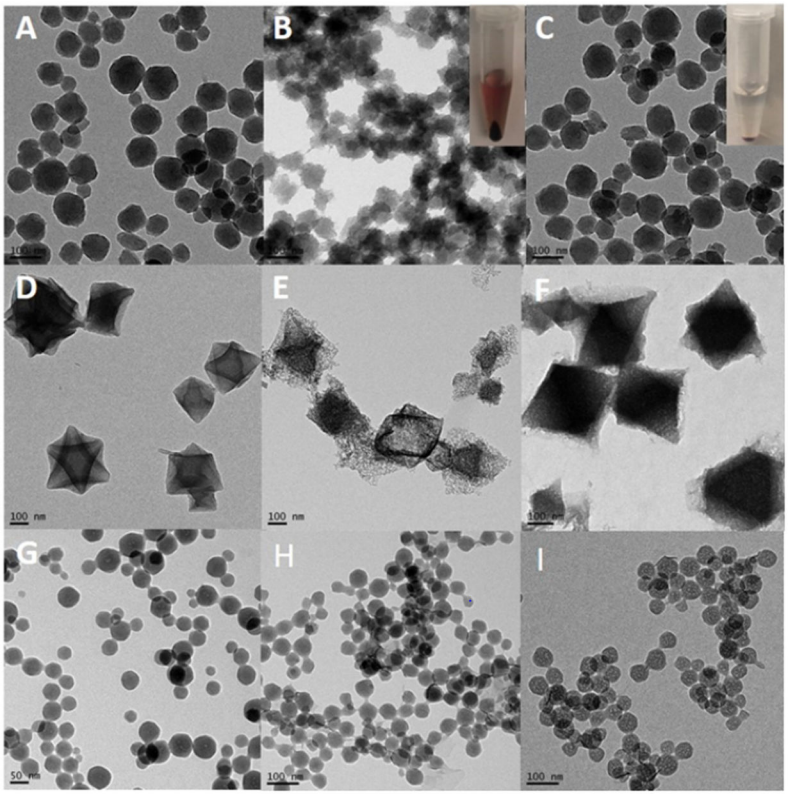

Fig. 1. Stability of MOF nanoparticles in different buffers.

(A), (D), and (G) are TEM images of ZrMOF, MIL-101 (Fe), and ZIF-8 nanoparticles in DMF. (B) TEM image of ZrMOF in 1X PBS for 1 hour. (C) TEM of ZrMOF-PAC in 1X PBS for 20 h. (E) TEM image of MIL-101 (Fe) in 1X PBS for 15 h. (F) TEM image of MIL-101 (Fe) in 1X PBS for 15 h. (H) TEM image of ZIF-8-PEG in sodium acetate buffer (pH = 5.5) for 1 h. (I) TEM image of ZIF-8-PEG in sodium acetate buffer (pH = 5.5) for 3 h. (ZIF-8 nanoparticles without polymer protection were dissolved completely and immediately when added to sodium acetate buffer (pH = 5.5)). Inset picture in (B) is the centrifugation result of ZrMOF in 1X PBS for 1 h. Inset picture in (C) is the centrifugation result of ZrMOF-PAC in 1x PBS for 1 h.

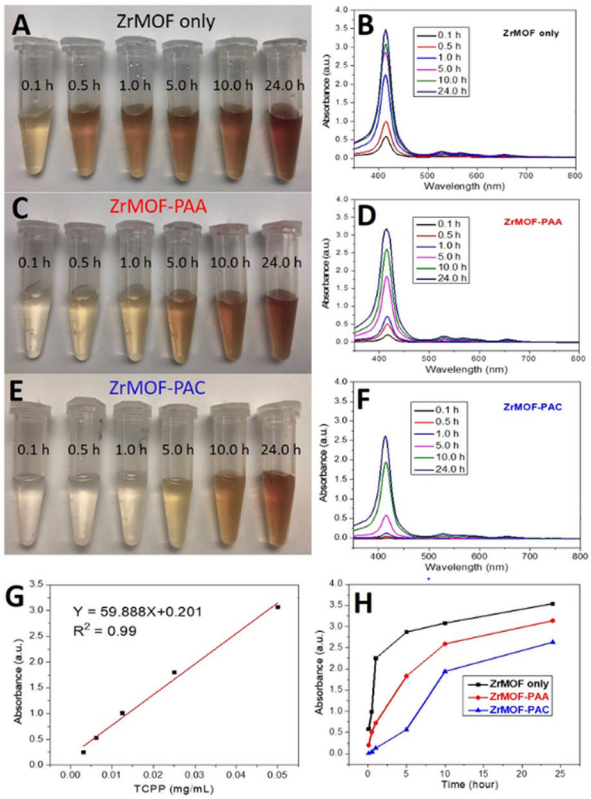

Fig. 2. Time-dependent stability study of ZrMOF, ZrMOF-PAA, and ZrMOF-PAC in phosphate buffer saline.

(A), (C), and (E) are digital camera pictures of the supernatant of ZrMOF, ZrMOF-PAA, and ZrMOF-PAC at different time points after being suspended in 1X PBS. (B), (D), and (F) are corresponding UV-vis spectrum of the dissociated TCPP in the supernatant after suspending ZrMOF, ZrMOF-PAA, and ZrMOF-PAC in 1X PBS for different periods of time (0.1, 0.5, 1, 5, 10, and 24 h). (G) Standard curve of TCPP in 1X PBS for TCPP quantification. (H) Dissociation comparison of ZrMOF, ZrMOF-PAA, and ZrMOF-PAC in 1X PBS.

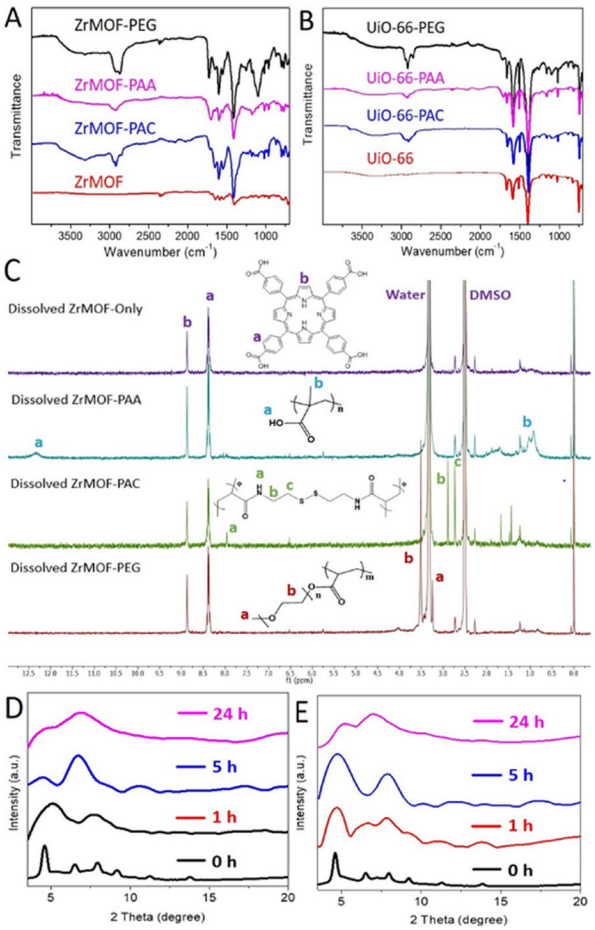

Fig. 3. Characterization of polymer-wrapped MOF nanoparticles.

Infrared spectra of ZrMOF (A) and UiO-66 (B) before and after polymerization with different ligands. (C)1H NMR spectra of the collected *in situ* polymer after decomposing the ZrMOF nanoparticles with PBS and dialysis. (D) Time-dependent stability of ZrMOF in PBS monitored by XRD. (E) Time-dependent stability of ZrMOF-PAC in PBS monitored by XRD.

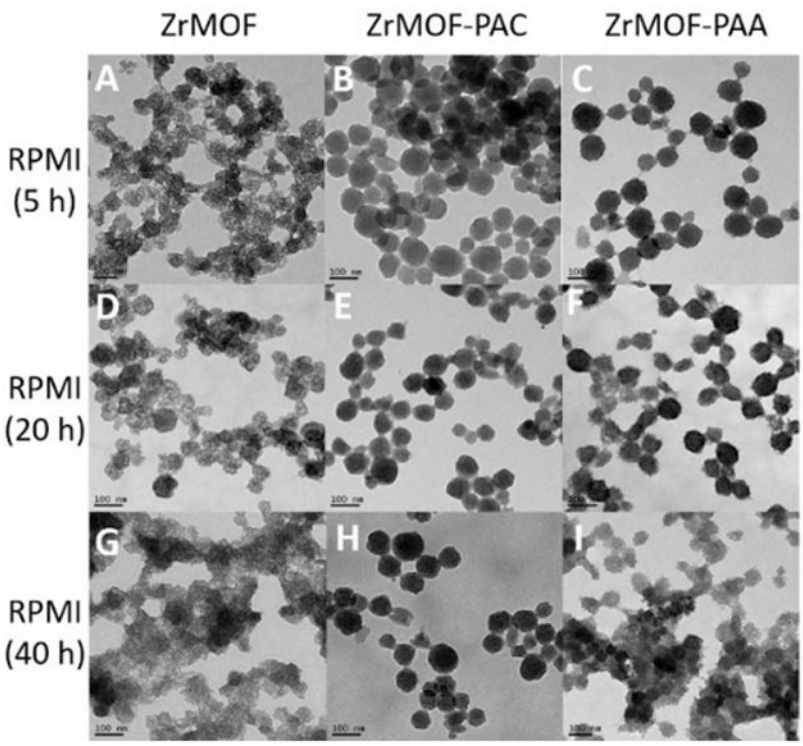

Fig. 4. Time-dependent stability of nanoscale MOFs in cell culture medium RPMI-1640.
(A), (D), and (G) are TEM pictures of ZrMOF after 5, 20, and 40 h in RPMI-1640. (B), (E), and (H) are TEM pictures of ZrMOF-PAC after 5, 20, and 40 h in RPMI-1640. (C), (F), and (I) are TEM pictures of ZrMOF-PAA after 5, 20, and 40 h in RPMI-1640. Scale bar: 100 nm.

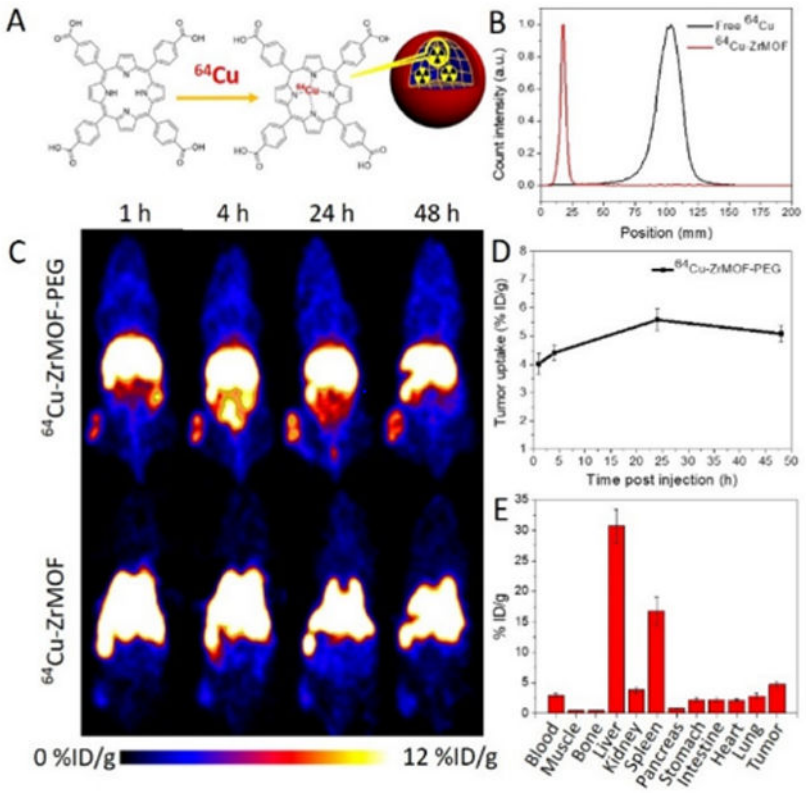

Fig. 5. ***In vivo*** **PET imaging of A431 tumor-bearing mice at different time points after intravenous injection of ^{64}Cu-ZrMOF-PEG nanoparticles.**

(A) Illustration of ^{64}Cu labeling in ZrMOF nanoparticles. (B) ITLC of free ^{64}Cu and ^{64}Cu-labeled ZrMOF-PEG nanoparticles. (C) Representative whole-body PET imaging at 1, 4, 24, and 48 h post-injection. (D) Quantitation of ^{64}Cu-ZrMOF-PEG nanoparticle accumulation in tumor based on decay-corrected PET images. (E) biodistribution of tumor and primary organs based on γ-counting.

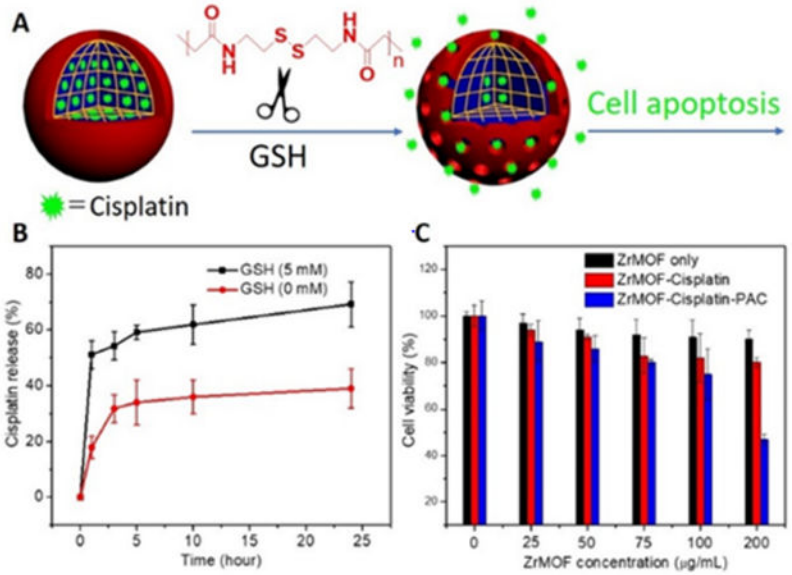

Fig. 6. GSH-responsive drug delivery from ZrMOF-PAC nanoparticles.

(A) illustration of cisplatin-loaded ZrMOF-PAC nanoparticles with GSH-responsive intracellular release. (B) *In vitro* cisplatin release from ZrMOF-PAC with and without GSH stimulus. (C) Cytotoxicity of GSH responsive cisplatin release from ZrMOF-PAC nanoparticles.

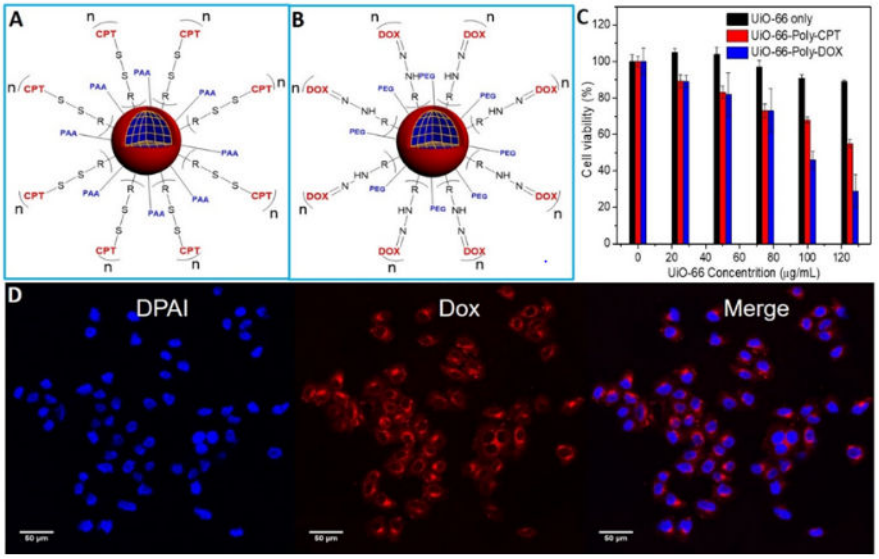

Fig. 7. Stimuli-responsive drug delivery system.

(A) GSH-responsive intracellular drug delivery model from UiO-66-poly-CPT. (B) Acidic pH-responsive intracellular drug delivery model from UiO-66-poly-Dox nanoparticles. (C) Cytotoxicity of pH-responsive UiO-66-poly-Dox and GSH-responsive UiO-66-poly-CPT nanoparticles. (D) Confocal imaging of UiO-66-poly-Dox uptake by U87MG cells.

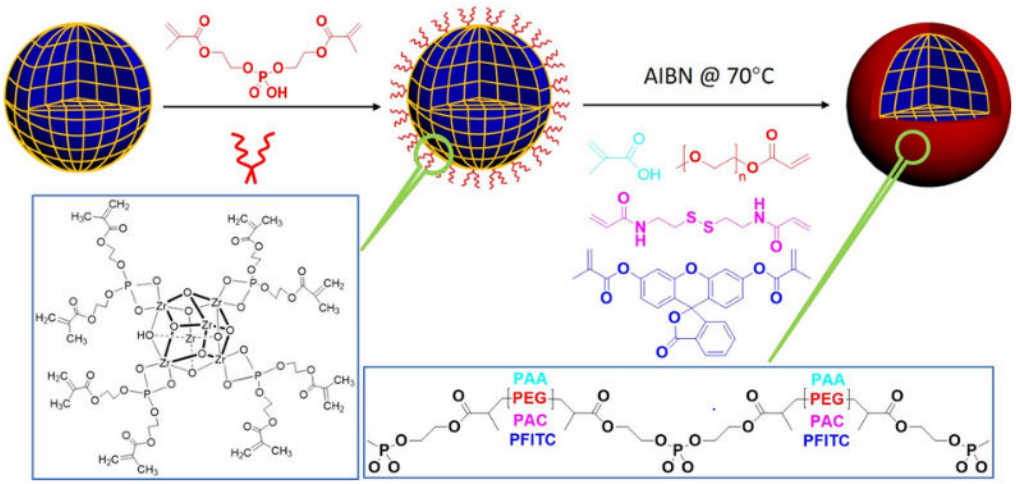

Scheme 1. Illustration of *in situ* polymerization on MOF nanoparticles.

Bis[2-(methacryloyloxy)ethyl] phosphate (BMAP) ligands were anchored on the surface of MOF nanoparticles first at room temperature, then different monomers were polymerized on the surface of MOF nanoparticles respectively initiated by AIBN at 65 °C in DMF.